

One-sided Outflows/Jets from Rotating Stars with Complex Magnetic Fields

R. V. E. Lovelace^{1*}, M. M. Romanova^{2†}, G. V. Ustyugova^{3‡}, A. V. Koldoba^{4§}

¹ Departments of Astronomy and Applied and Eng. Phys. Cornell University, Ithaca, NY 14853, USA

² Department of Astronomy, Cornell University, Ithaca, NY 14853, USA

³ Keldysh Institute of Applied Mathematics, Russian Academy of Sciences, Moscow, Russia

⁴ Institute for Mathematical Modeling, Russian Academy of Sciences, Moscow, Russia

30 October 2018

ABSTRACT

We investigate the generation of intrinsically asymmetric or *one-sided* outflows or jets from disk accretion onto rotating stars with complex magnetic fields using axisymmetric (2.5D) magnetohydrodynamic simulations. The intrinsic magnetic field of the star is assumed to consist of a superposition of an aligned dipole and an aligned quadrupole in different proportions. The star is assumed to be rapidly rotating in the sense that the star’s magnetosphere is in the propeller regime where strong outflows occur. Our simulations show that for conditions where there is a significant quadrupole component in addition to the dipole component, then a dominantly *one-sided* conical wind tends to form on the side of the equatorial plane with the larger value of the intrinsic axial magnetic field at a given distance. For cases where the quadrupole component is absent or very small, we find that dominantly one-sided outflows also form, but the direction of the flow “flip-flops” between upward and downward on a time-scale of ~ 30 days for a protostar. The average outflow will thus be symmetrical. In the case of a pure quadrupole field we find symmetric outflows in the upward and downward directions.

Key words: accretion, accretion discs; MHD; stars: magnetic fields

1 INTRODUCTION

There is clear evidence, mainly from Hubble Space Telescope (HST) observations, of the asymmetry between the approaching and receding jets from a number of young stars. The objects include the jets in HH 30 (Bacciotti et al. 1999), RW Aur (Woitas et al. 2002), TH 28 (Coffey et al. 2004), and LkH α 233 (Pererin & Graham 2007). Specifically, the radial speed of the approaching jet may differ by a factor of two from that of the receding jet. For example, for RW Aur the radial redshifted speed is ~ 100 km/s whereas the blueshifted radial speed is ~ 175 km/s. The mass and momentum fluxes are also significantly different for the approaching and receding jets in a number of cases. Of course, it is possible that the observed asymmetry of the jets could be due to say differences in the gas densities on the two sides of the source. Here, we investigate the case of intrinsic asymmetry where the asymmetry of outflows is connected with asymmetry of the star’s magnetic field.

There is substantial observational evidence that young stars often have *complex* magnetic fields consisting of dipole, quadrupole, and higher order poles possibly misaligned with respect to each other and the rotation axis (Donati et al. 2007a, b; 2008; Jardine et al. 2002). Analysis of mater flow around stars with realistic fields have shown that a fraction of the star’s magnetic field lines are open and may carry outflows (e.g., Gregory et al. 2006).

A number of global 3D MHD simulations have been done of disk accretion onto rotating stars with complex magnetic fields. The star’s intrinsic field may be a superposition of aligned or misaligned dipole and quadrupole fields (Long, Romanova, & Lovelace 2007, 2008), or a superposition of dipole and octupole field components (Long, Romanova, Lamb 2009; Romanova et al. 2009a; Long et al. 2010). These simulations were focused on accretion processes. To study the outflows from these systems requires a much lower coronal density than assumed in these works. Intermittent outflows from the disk-magnetosphere boundary have been found in axisymmetric simulations in cases where the star has a dipole magnetic field and where symmetry about the equatorial plane was assumed (e.g., Goodson, Winglee, & Böhm 1997; Goodson, Böhm, & Winglee 1999).

* E-mail: RVL1@cornell.edu

† E-mail: romanova@astro.cornell.edu

‡ E-mail: ustyugg@rambler.ru

§ E-mail: koldoba@rambler.ru

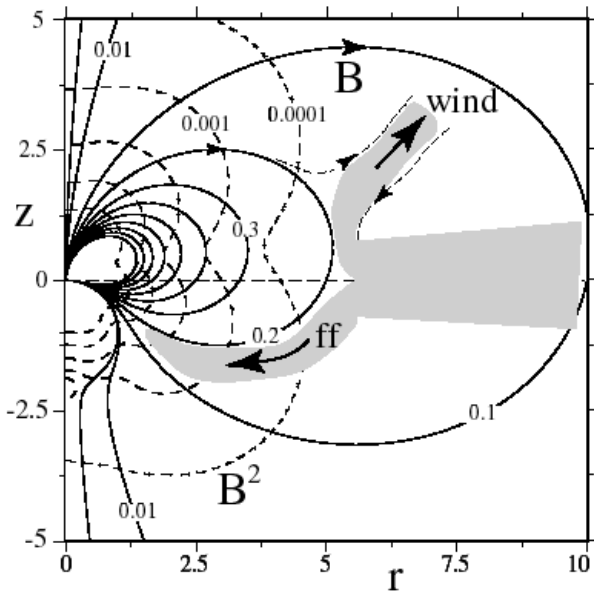


Figure 1. The magnetic field lines $\Psi(r, z) = \text{const}$ and constant magnetic pressure lines for the case of an aligned dipole and quadrupole field where the flux function is $\Psi = \mu_d r^2/R^3 + (3/4)\mu_q z r^2/R^5$, where $R^2 = r^2 + z^2$ and μ_d is the dipole moment and μ_q is the quadrupole moment. Roughly, μ_q/μ_d is the distance at which dipole and quadrupole fields are equal. The funnel flow (ff) and the wind in this figure are suggested. The dashed lines are constant values of B^2 .

In long-time axisymmetric (2.5D) simulations, long-lasting outflows were obtained first in the propeller regime where the star spins rapidly (Romanova et al. 2005; Ustyugova et al. 2006), and subsequently in the general case by Romanova et al. (2009b; hereafter R09). In the propeller regime the outer part of the star's magnetosphere - the magnetopause - rotates more rapidly than the Keplerian rate of the accretion disk (Lovelace, Romanova, & Bisnovaty-Kogan 1999). Simulations show that most of the matter outflow goes into conical-shape winds from the inner part of the disk. This wind resembles the X-wind model (Shu et al. 1994), but there are a number of important differences discussed in R09.

The present work investigates the nature of outflows from a star with a *complex magnetic field*. As a first step we consider superposition of an dipole and a quadrupole field components both aligned with the rotation axis of the star and of the disk. For such a configuration the magnetic field is *not* symmetric about the equatorial plane. This can give rise to one-sided or asymmetric magnetically driven outflows (Wang, Sulkanen, & Lovelace 1992). Figure 1 shows the nature of a combined vacuum dipole plus quadrupole field components. In this case we have sketched an extreme possibility where there is a conical wind from the top side of the disk but no outflow from the bottom side, only a funnel flow marked ff.

In this paper we present results out systematic MHD simulations of the formation of conical winds for the axisymmetric dipole/quadrupole field combinations following the approach of R09 where conical winds are found to form at the disk-magnetosphere boundary. The new aspect of the present work is that the outflows are *not* required to be symmetrical about the equatorial plane.

Section 2 of the paper describes the different aspects of the simulation model. Section 3 discusses the results of the simulations We will quantify the asymmetry of the velocities of the top/bottom jets as well as the asymmetry of the mass and momentum fluxes for different quadrupole/dipole field strengths, different disk accretion rates, and different stellar rotation rates. Section 4 gives the conclusions of this work.

2 SIMULATION MODEL

We investigate the formation of one-sided or asymmetric jets using a set of axisymmetric numerical simulations. The arrangement of the problem is similar to that described by Ustyugova et al. (2006, hereafter - U06). However, in contrast with U06, the simulations were performed in the *entire* simulation region *without* assuming symmetry about the equatorial plane. Below we describe the main aspects of the simulation model and point out the new aspects of the present model.

2.1 Basic Equations

Outside of the disk the flow is described by the equations of ideal MHD. Inside the disk the flow is described by the equations of viscous, resistive MHD. In an inertial reference frame the equations are

$$\frac{\partial \rho}{\partial t} + \nabla \cdot (\rho \mathbf{v}) = 0, \quad (1)$$

$$\frac{\partial (\rho \mathbf{v})}{\partial t} + \nabla \cdot \mathcal{T} = \rho \mathbf{g}, \quad (2)$$

$$\frac{\partial \mathbf{B}}{\partial t} - \nabla \times (\mathbf{v} \times \mathbf{B}) + \nabla \times (\eta_t \nabla \times \mathbf{B}) = 0, \quad (3)$$

$$\frac{\partial (\rho S)}{\partial t} + \nabla \cdot (\rho S \mathbf{v}) = Q. \quad (4)$$

Here, ρ is the density and S is the specific entropy; \mathbf{v} is the flow velocity; \mathbf{B} is the magnetic field; \mathcal{T} is the momentum flux-density tensor; Q is the rate of change of entropy per unit volume; and $\mathbf{g} = -(GM/r^2)\hat{\mathbf{r}}$ is the gravitational acceleration due to the star, which has mass M . The total mass of the disk is assumed negligible compared to M . The plasma is considered to be an ideal gas with adiabatic index $\gamma = 5/3$, and $S = \ln(p/\rho^\gamma)$. We use spherical coordinates (r, θ, ϕ) with θ measured from the symmetry axis. The condition for axisymmetry is $\partial/\partial\phi = 0$. The equations in spherical coordinates are given in U06.

The stress tensor \mathcal{T} and the treatment of viscosity and diffusivity are described in the Appendix of R09. Briefly, both the viscosity and the magnetic diffusivity of the disk plasma are considered to be due to turbulent fluctuations of the velocity and the magnetic field. We adopt the standard hypothesis where the microscopic transport coefficients are replaced by turbulent coefficients. We use the α -model of Shakura and Sunyaev (1973) where the coefficient of the turbulent kinematic viscosity $\nu_t = \alpha_v c_s^2/\Omega_K$, where c_s is the isothermal sound speed and $\Omega_K(r)$ is the Keplerian angular velocity. Similarly, the coefficient of the turbulent magnetic diffusivity $\eta_t = \alpha_d c_s^2/\Omega_K$. Here, α_v and α_d are dimensionless coefficients which are treated as parameters of the model.

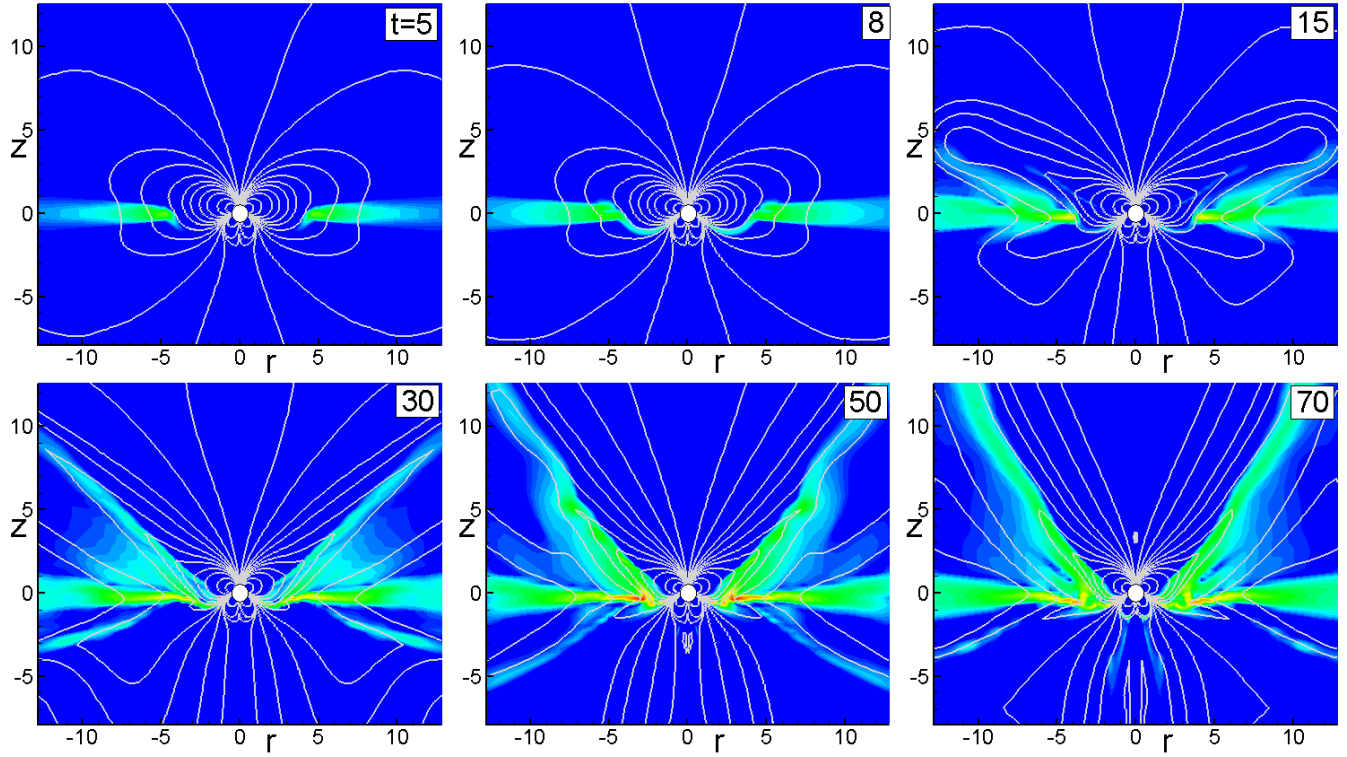


Figure 2. Development of an asymmetric jet in the main case ($\bar{\mu}_d = 10$, $\bar{\mu}_q = 20$). The color background shows the matter flux-density. The lines are the poloidal field lines. The simulations are shown at different times t , which is measured in periods of rotation of the disk at $r = 1$.

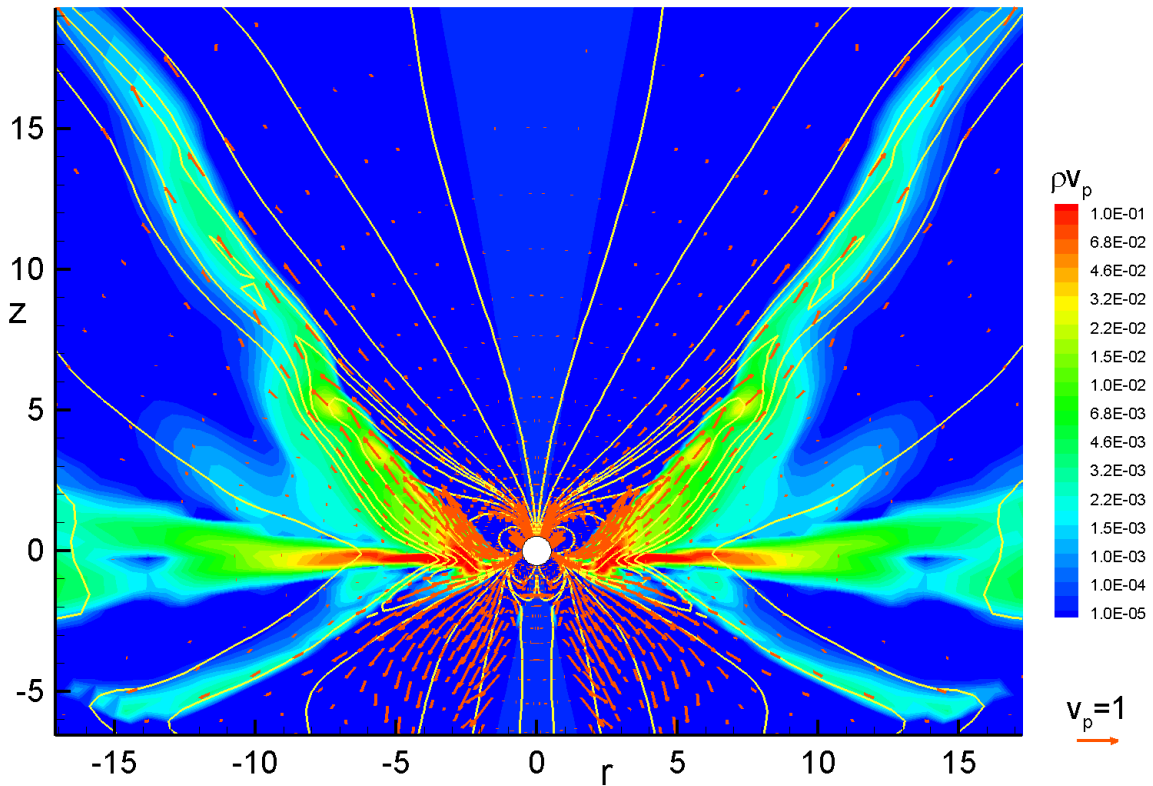


Figure 3. Enlarged snapshot of the outflow in the main case ($\bar{\mu}_d = 10$, $\bar{\mu}_q = 20$) at $t = 50$. The color background shows the matter flux-density and the lines are the poloidal field lines. The vectors show the poloidal velocity.

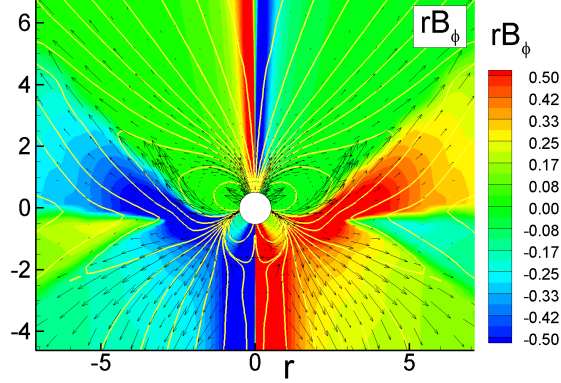


Figure 4. The color background shows $rB_\phi(r, z)$ at $t = 50$, which is proportional to the poloidal current flow through a circular disk of radius r at a distance z . The lines are poloidal field lines and the arrows show the poloidal velocity. For this case $\tilde{\mu}_d = 10$ and $\tilde{\mu}_q = 20$.

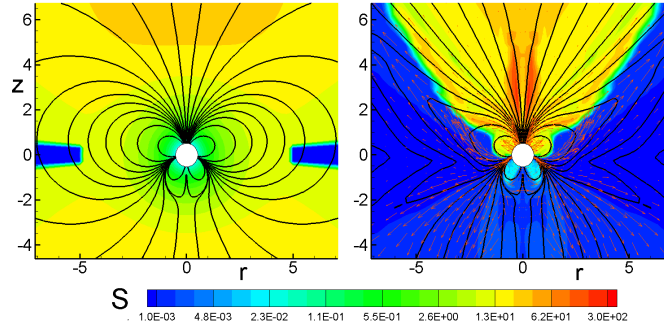


Figure 5. The color background shows the distribution of the specific entropy S . The left-hand panel shows initial distribution and the right-hand panel shows the distribution at $t = 50$. The lines are poloidal field lines. For this case $\tilde{\mu}_d = 10$ and $\tilde{\mu}_q = 20$.

2.2 Magnetic field of star

We consider the superposition of aligned dipole and quadrupole field components,

$$\mathbf{B} = \mathbf{B}_d + \mathbf{B}_q, \quad (5)$$

where

$$\begin{aligned} \mathbf{B}_d &= \frac{3\mu_d(\hat{\boldsymbol{\mu}}_d \cdot \hat{\mathbf{r}})\hat{\mathbf{r}}}{|\mathbf{r}|^3} - \frac{\mu_d\hat{\boldsymbol{\mu}}_d}{|\mathbf{r}|^3}, \\ \mathbf{B}_q &= \frac{3\mu_q(5(\hat{\boldsymbol{\mu}}_q \cdot \hat{\mathbf{r}})^2 - 1)\hat{\mathbf{r}}}{4|\mathbf{r}|^4} - \frac{3\mu_q(\hat{\boldsymbol{\mu}}_q \cdot \hat{\mathbf{r}})\hat{\boldsymbol{\mu}}_q}{2|\mathbf{r}|^4}. \end{aligned} \quad (6)$$

Here, \mathbf{B}_d and \mathbf{B}_q are the magnetic fields of the dipole and quadrupole components with μ_d and μ_q the magnetic moments. Also, $\hat{\mathbf{r}}$, $\hat{\boldsymbol{\mu}}_d$ and $\hat{\boldsymbol{\mu}}_q$ are unit vectors for the position and the direction of the dipole and quadrupole moments, respectively. For the considered conditions $\hat{\boldsymbol{\mu}}_d$ and $\hat{\boldsymbol{\mu}}_q$ are in the z -direction. The combined dipole/quadrupole field can be expressed in terms of the flux function $\Psi = \mu_d r^2/R^3 + (3/4)\mu_q z r^2/R^5$, where the field lines correspond to $\Psi(r, z) = \text{const}$. Here, we briefly use cylindrical coordinates (r, ϕ, z) , with $R^2 = r^2 + z^2$, $B_r = -(1/r)\partial\Psi/\partial z$, and $B_z = (1/r)\partial\Psi/\partial r$.

2.3 Reference Units

The MHD equations are solved in dimensionless form so that the results can be readily applied to different accreting stars

(see §7). We take the reference mass M_0 to be the mass M of the star. The reference radius is taken to be twice the radius of the star, $R_0 = 2 \times R_*$. The reference velocity is $v_0 = (GM/R_0)^{1/2}$, and the reference angular velocity $\Omega_0 = 1/t_0$. We measure time in units of $P_0 = 2\pi t_0$, which is the Keplerian rotation period of the disk at $r = R_0$. In the plots we use the dimensionless time $T = t/P_0$.

The dimensionless dipole and quadrupole magnetic moments are

$$\tilde{\mu}_d \equiv \frac{\mu_d}{B_0 R_0^3}, \quad \tilde{\mu}_q \equiv \frac{\mu_q}{B_0 R_0^4}, \quad (7)$$

where B_0 is the reference magnetic field. Taking into account that $\mu_d = B_{d*} R_*^3 = B_0 R_0^3 \tilde{\mu}_d$, we find $B_0 = B_{d*} (R_*/R_0)^3 / \tilde{\mu}_d$, where B_{d*} is the equatorial dipole magnetic field strength on the surface of the star.

The reference density is taken to be $\rho_0 = B_0^2/v_0^2$. The reference pressure is $p_0 = B_0^2$. The reference temperature is $T_0 = p_0/\mathcal{R}\rho_0 = v_0^2/\mathcal{R}$, where \mathcal{R} is the gas constant. The reference accretion rate is $\dot{M}_0 = \rho_0 v_0 R_0^2$. The reference energy flux is $\dot{E}_0 = \dot{M}_0 v_0^2$. The reference angular momentum flux is $\dot{L}_0 = \dot{M}_0 v_0 R_0$.

The reference units are defined in such a way that the dimensionless MHD equations have the same form as the dimensional ones, equations (1)-(4) (for such dimensionalization we put $GM = 1$ and $\mathcal{R} = 1$). Table 1 shows examples of reference variables for different stars. We solve the MHD equations (1)-(4) using normalized variables: $\tilde{\rho} = \rho/\rho_0$, $\tilde{v} = v/v_0$, $\tilde{B}_d = B_d/B_0$, $\tilde{B}_q = B_q/B_0$ etc. Most of the plots

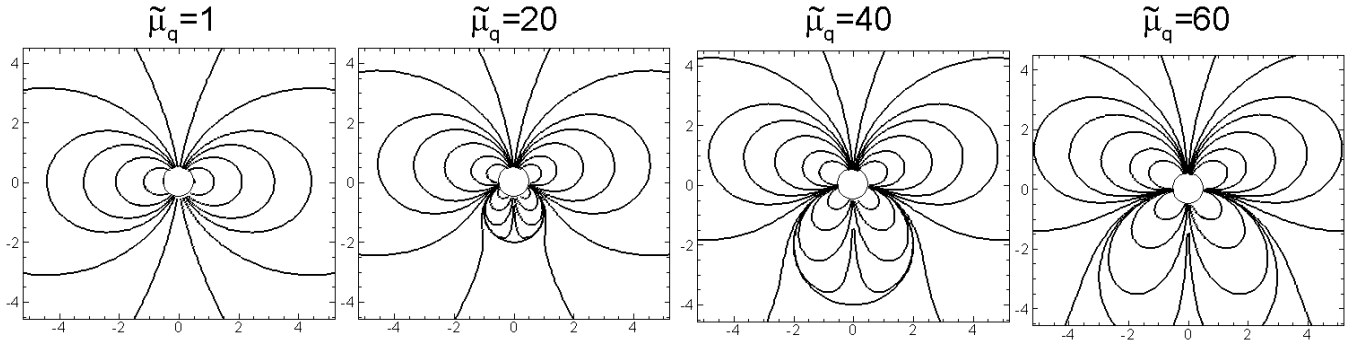


Figure 6. The figure shows the initial poloidal field lines for a fixed dipole moment $\mu_d = 10$ and different quadrupolar moments, $\mu_q = 0, 20, 30, 40$. The field lines have the same value of the flux function in all plots.

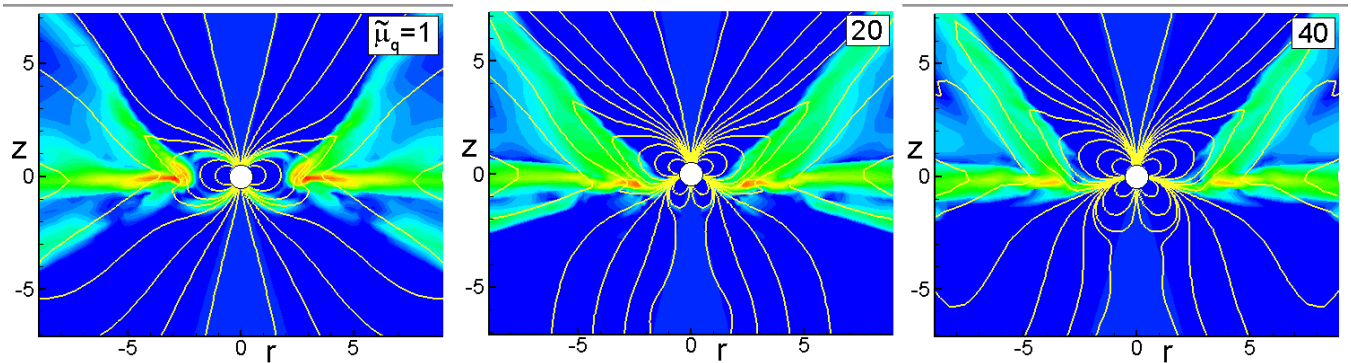


Figure 7. Outflows for different quadrupole strengths μ_q but the same dipole component $\mu_d = 10$ at $t = 50$. The color background shows the matter flux-density distribution. The lines are poloidal magnetic field lines.

show the normalized variables (with the tildes implicit). To obtain dimensional values one needs to multiply values from the plots by the corresponding reference values from Table 1.

2.4 Initial and Boundary Conditions

The initial and boundary conditions are the same as those used in U06. Here, we summarize these conditions.

Initial Conditions. A star of mass M is located at the origin of the coordinate system. A cold disk and hot corona are initialized in the simulation region. The disk is of low-temperature T_d and high-density ρ_d . The corona is of high-temperature $T_c \gg T_d$, and low-density $\rho_c \ll \rho_d$ and it fills all other space but the disk. The disk extends inward to a radius $r_d = 5$ and rotates with Keplerian angular velocity $\omega \approx \Omega_K$. In reality, it is slightly sub-Keplerian, $\Omega(\theta = \pi/2) = \kappa\Omega_K$ ($\kappa = 1 - 0.003$), due to which the density and pressure decrease towards the periphery. Initially, at any cylindrical radius r from the rotation axis, we rotate the corona and the disk at the same angular rate. This avoids a jump discontinuity of the angular velocity of the plasma at the boundary between the disk and the corona. Inside the cylinder $r \leq r_d$, the matter of the corona rotates rigidly with angular velocity $\Omega(r_d) = \kappa(GM/r_d^3)^{1/2}$. For a gradual start-up we change the angular velocity of the star from its initial value $\Omega(r_d) = 5^{-3/2} \approx 0.09$ ($r_d = 5$) to a final value of $\Omega_* = 1$ over the course of three Keplerian rotation periods at $r = 1$.

In most simulation runs we fix the dipole moment of the star as $\tilde{\mu}_d = 10$ and vary the quadrupole moment as

$\tilde{\mu}_q = 0, 1, 10, 20, 30, 40, 60$. We also have test cases of $\tilde{\mu}_d = 0$ and $\tilde{\mu}_q = 20, 60$. The angular velocity of the star in the propeller regime is $\Omega_* = 1$ and this corresponds to the corotation radius of $r_{cor} = 1$. The initial density in the disk at the fiducial point (at the inner edge) is $\rho_d = 1$, initial density in the corona $\rho_c = 0.0003$. The gas in the corona is hot with initial temperature $T_c = 1$ and the disk is cold with temperature $T_d = (\rho_c/\rho_d)T_c = 3 \times 10^{-4}$. There is initial pressure equilibrium at the disk-corona boundary.

The coefficients of viscosity and diffusivity are taken to be $\alpha_v = 0.3$ and $\alpha_d = 0.1$ (as in R09).

Boundary conditions. The boundary conditions at the inner boundary $r = R_{in}$ are the following: The frozen-in condition is applied to the poloidal component \mathbf{B}_p of the field, such that B_r is fixed while B_θ and B_ϕ obey “free” boundary conditions, $\partial B_\theta/\partial r = 0$ and $\partial B_\phi/\partial r = 0$. The density, pressure, and entropy also have free boundary conditions, $\partial(\dots)/\partial r = 0$. The velocity components are calculated using free boundary conditions. Then, the velocity vector is adjusted to be parallel to the magnetic field vector in the coordinate system rotating with a star. Matter always flows inward at the star’s surface. Outflow of a wind from the stellar surface is not considered in this work. The boundary conditions at the external boundary $r = R_{out}$ in the coronal region $0 < \theta < \theta_{d1}$ and $\theta_{d2} < \theta \leq \pi$ are free for all hydrodynamic variables. Here, θ_{d1} corresponds to the top surface of the and θ_{d2} to the bottom surface. We prevent matter from flowing into the simulation region from this part of the boundary. We solve the transport equation for the flux function Ψ so that the magnetic flux

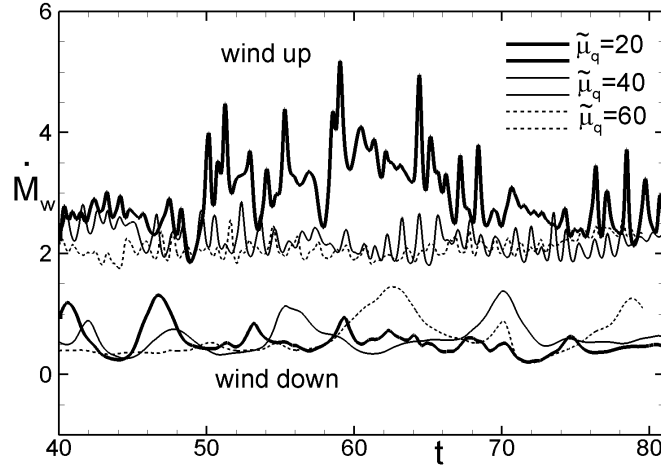


Figure 8. Matter fluxes through a hemispherical surface of radius $r = 10$ above the equatorial plane (top set of curves) and below the equatorial plane (bottom set of curves) for cases with $\tilde{\mu}_d = 10$ and different quadrupole moments of $\tilde{\mu}_q = 20, 40, 60$.

	Protostars	CTTSs	Brown dwarfs	White dwarfs	Neutron stars
$M(M_\odot)$	0.8	0.8	0.056	1	1.4
R_*	$2R_\odot$	$2R_\odot$	$0.1R_\odot$	5000 km	10 km
R_0 (cm)	2.8×10^{11}	2.8×10^{11}	1.4×10^{10}	1.0×10^9	2×10^6
v_0 (cm s $^{-1}$)	1.95×10^7	1.95×10^7	1.6×10^7	3.6×10^8	9.7×10^9
P_0	1.04 days	1.04 days	0.05 days	17.2 s	1.3 ms
B_{d*} (G)	3.0×10^3	10^3	2.0×10^3	10^6	10^9
B_0 (G)	37.5	12.5	25.0	1.2×10^4	1.2×10^7
ρ_0 (g cm $^{-3}$)	3.7×10^{-12}	4.1×10^{-13}	1.4×10^{-12}	1.2×10^{-9}	1.7×10^{-6}
$\dot{M}_0(M_\odot \text{yr}^{-1})$	1.8×10^{-7}	2.0×10^{-8}	1.8×10^{-10}	1.3×10^{-8}	2.0×10^{-9}
\dot{E}_0 (erg s $^{-1}$)	2.1×10^{33}	2.4×10^{32}	2.5×10^{30}	5.7×10^{34}	6.0×10^{36}
\dot{L}_0 (erg s $^{-1}$)	3.1×10^{37}	3.4×10^{36}	1.7×10^{33}	1.6×10^{35}	1.2×10^{33}
T_d (K)	2293	4586	5274	1.6×10^6	1.1×10^9
T_c (K)	2.3×10^6	4.6×10^6	5.3×10^6	8.0×10^8	5.6×10^{11}

Table 1. Reference values for different types of stars. We choose the mass M , radius R_* , equatorial dipole magnetic field B_{d*} of the star and derive the other reference values for the case $\tilde{\mu}_d = 10$ (see §2.3). To apply the simulation results to a particular star one needs to multiply the dimensionless values from the plots by the reference values from this table.

flows out of the region together with matter. If the matter has a tendency to flow back in, then we fix Ψ . In the disk region, restricted by two values of θ ($\theta_{a1} < \theta < \theta_{a2}$), we fix the density at $\rho = \rho_d$, and establish a slightly sub-Keplerian velocity, $\Omega_d = \kappa\Omega(r_d)$, where $\kappa = 1 - 0.003$ so that matter flows into the simulation region through the boundary. The inflowing matter has a fixed magnetic flux which is very small because $R_{out} \gg R_{in}$.

The system of MHD equations (1-4) was integrated numerically using the Godunov-type numerical scheme (see Appendix of R09). The simulations were done in the region $R_{in} \leq r \leq R_{out}$, $0 \leq \theta \leq \pi$. The grid is uniform in the θ -direction. The size steps in the radial direction were chosen so that the poloidal-plane cells were curvilinear rectangles with approximately equal sides. A typical region for investigation of asymmetric winds was $1 \leq r \leq 40$, with grid resolution $N_r \times N_\theta = 104 \times 80$ cells. The simulation domain has 13 slices in the radial direction and 10 slices in θ direction. Each simulation run takes 4 – 12 days on 130 processors of the NASA high-performance facilities. Cases with stronger quadrupole component require longer simulations. The simulation time increases with increase of the quadrupole moment, and hence

the longest simulations are those at $\tilde{\mu}_q = 60$. Test runs were also performed at the lower grid of 80×60 and higher grid of 160×120 which show similar results (approximately the same matter flux onto the star and into the winds), though the latter grids requires more computer resources. Simulations with the grid of 80×60 were used for a number of exploratory runs.

3 RESULTS

3.1 Properties of one-sided outflows

Here, we chose one case with intermediate parameters: $\mu_d = 10$, $\mu_q = 20$, call it “the main case”, and show it in greater detail compared with other cases. Fig 2 shows formation of asymmetric outflows. One can see that initially, at $t = 5 - 8$, matter start to accrete onto the star along the shortest path, towards the quadrupolar belt, which is below the equator. Later, at $t \approx 15$, the disk matter diffused through the external closed field lines of the top and bottom parts of the magnetosphere, these lines inflated, and the conical-type wind start to blow along these field lines. Most of matter outflows from the

top side of the disk, where the magnetic field is stronger. Outflows are episodic but quasi-steady on average. The episodic nature is connected with accumulation of matter near the closed magnetosphere, diffusion through closed field lines, inflation of these lines, outburst to the wind and enhanced accretion onto the star (see also Goodson & Winglee 1997; U06; R09). Fig 3 shows larger view of typical, well-developed outflows at $t = 50$. One can see that outflows are more powerful on the top part, and much less powerful on the bottom.

The mechanism of the outflow formation is similar to that in cases of conical winds (R09): The magnetic flux of the star is pushed towards the star and compressed by the disk so that the poloidal field lines are always inclined relative to the disk. In addition, the rotating magnetosphere acts to make the field lines to rotate with a super-Keplerian velocity. These field lines thread the corona which rotates more slowly. Consequently there is a strong winding-up of the field lines just above the disk. Hence a strong magnetic force appears, $F_m = -\nabla(r^2 B_\phi^2)$, which drives matter down the gradient of the magnetic pressure (Lovelace, Berk & Contopoulos 1991). Fig 4 shows the poloidal current through a disk of radius r , $I_p \propto r B_\phi$. One can see that matter flows to the conical-type winds and is driven by the magnetic force. Ohmic heating is included in our code, but it does not have a significant role in the jet launching. Figure 5 shows the initial distribution of the specific entropy and that at $t = 50$. One can see that the low-entropy (cold) matter from the disk flows to the winds above and below the disk. On the top side of the disk this cold matter pushes the hot coronal gas towards the axis. On the bottom side of the disk, the hot coronal gas is pushed away and is gradually replaced by cold gas from the disk.

3.2 One-sided outflows for different quadrupole moments

In this section we compare asymmetric outflows obtained in a set of simulations where we fixed the dipole component of the field at $\tilde{\mu}_d = 10$ and varied the quadrupolar component from very small up to very large values: $\tilde{\mu}_q = 1, 10, 20, 30, 40, 60$. Figure 6 shows an initial magnetic field distribution in a number of cases. Figure 6 shows that at $\tilde{\mu}_q = 1$ the quadrupole component is very small and the magnetic field is almost pure dipole field, while for $\tilde{\mu}_q = 40, 60$ the quadrupole field dominates. Figure 7 shows asymmetric outflows at $t = 50$. One can see that in all cases most of the matter outflows above the disk, to the side where the intrinsic magnetic field is stronger. At the same time there is a much weaker matter flux from the other side of the disk.

We calculated the matter fluxes to outflows through a spherical surface of radius $r = 10$

$$\dot{M} = \int d\mathbf{S} \cdot \rho \mathbf{v}_p, \quad (8)$$

where $d\mathbf{S}$ is the surface area element directed outward. Figure 8 shows matter fluxes above and below the disk for cases with different $\tilde{\mu}_q$. One can see that the main, upward outflows, have similar matter fluxes for $\tilde{\mu}_q = 40$ and $\tilde{\mu}_q = 60$, while at lower quadrupole moment $\tilde{\mu}_q = 20$ matter flux is higher. The matter fluxes of the downward outflows (bottom set of curves in Fig. 8) are similar for all three cases and are 4 – 8 times smaller than the main, upward outflows.

3.3 Comparison of magnetic moments

Below, we discuss the relative strengths of the dipole and quadrupole components of the field. For this it is useful to consider the dipole and quadrupole field components in the equatorial plane, $B_{dz} = -\mu_d/r^3$ and $B_{qr} = -3\mu_q/4r^4$. The radius at which $|B_{dz}| = |B_{qr}|$ is

$$r_{eq} = \frac{3}{4} \frac{\mu_q}{\mu_d}, \quad \text{or} \quad r_{eq} = \frac{3}{4} \frac{\tilde{\mu}_q}{\tilde{\mu}_d} R_0 = \frac{3}{2} \frac{\tilde{\mu}_q}{\tilde{\mu}_d} R_*, \quad (9)$$

where we took into account that $R_0 = 2R_*$. We can estimate this radius for all cases above where $\tilde{\mu}_d = 10$ and quadrupolar moments, $\tilde{\mu}_q = 1, 10, 20, 30, 40, 60$. We obtain: $\tilde{r}_{eq} = (0.15, 1.5, 3.0, 4.5, 6.0, 9.0)R_*$. Hence, the quadrupole component is dynamically important in all cases, except $\tilde{\mu}_q = 1$, and is expected to influence, e.g., the matter flow around the star at $r > r_{eq}$ (Long et al. 2009, 2010; Romanova et al. 2009). However, we see that the quadrupole component determines the “one-sidedness” and the direction of the matter outflow even for very small values, such as of $\tilde{\mu}_q = 1$.

3.4 Symmetric Outflows for a pure quadrupole field

We performed simulations of outflows in the case of a pure quadrupole field with $\tilde{\mu}_q = 40, 60$ ($\tilde{\mu}_d = 0$). Figure 11 shows simulation results at $t = 50$ for case with $\tilde{\mu}_q = 60$. In this case the outflows are almost symmetric about the equatorial plane. However, in a test case with very small dipole magnetic field, $\tilde{\mu}_d = 1$, we found that the flow is one-sided and matter flows towards the direction of the larger intrinsic magnetic field.

3.5 “Flip-flop” of Outflows for a pure dipole field

For a pure dipole field, the outflows behaved in an unexpected way. In past simulations the MHD equations were solved only in the upper half space and it was *assumed* that the full flow was given by reflecting the top flow about the equatorial plane (U06; R09). However, in the present work we calculate the disk and outflows in the entire space above and below the equatorial plane. We discover that during a brief initial time, $t \lesssim 15$, the outflows are symmetric about the equatorial plane (see fig. 9, top left panels). However, later the outflows become strongly asymmetric with the direction of the main flow downward, which is an opposite to that of cases with quadrupolar component. Later, the main outflow changed its direction and matter started to flow upward. Later, the direction changed again (see fig. 9). The matter fluxes calculated through hemispherical surfaces with radius $r = 10$ above and below the disk also show this “flip-flop” behavior. The time-scale between the reversal of the direction of outflows is about 30 rotation periods. For CTTs this is about 30 days.

4 CONCLUSIONS

We performed axisymmetric MHD simulations of disk accretion onto rotating magnetized stars. The star’s intrinsic magnetic field was assumed to consist of a superposition of aligned dipole and quadrupole components. This field configuration is *not* in general symmetric about the equatorial plane. Thus the calculations must be done in both the upper

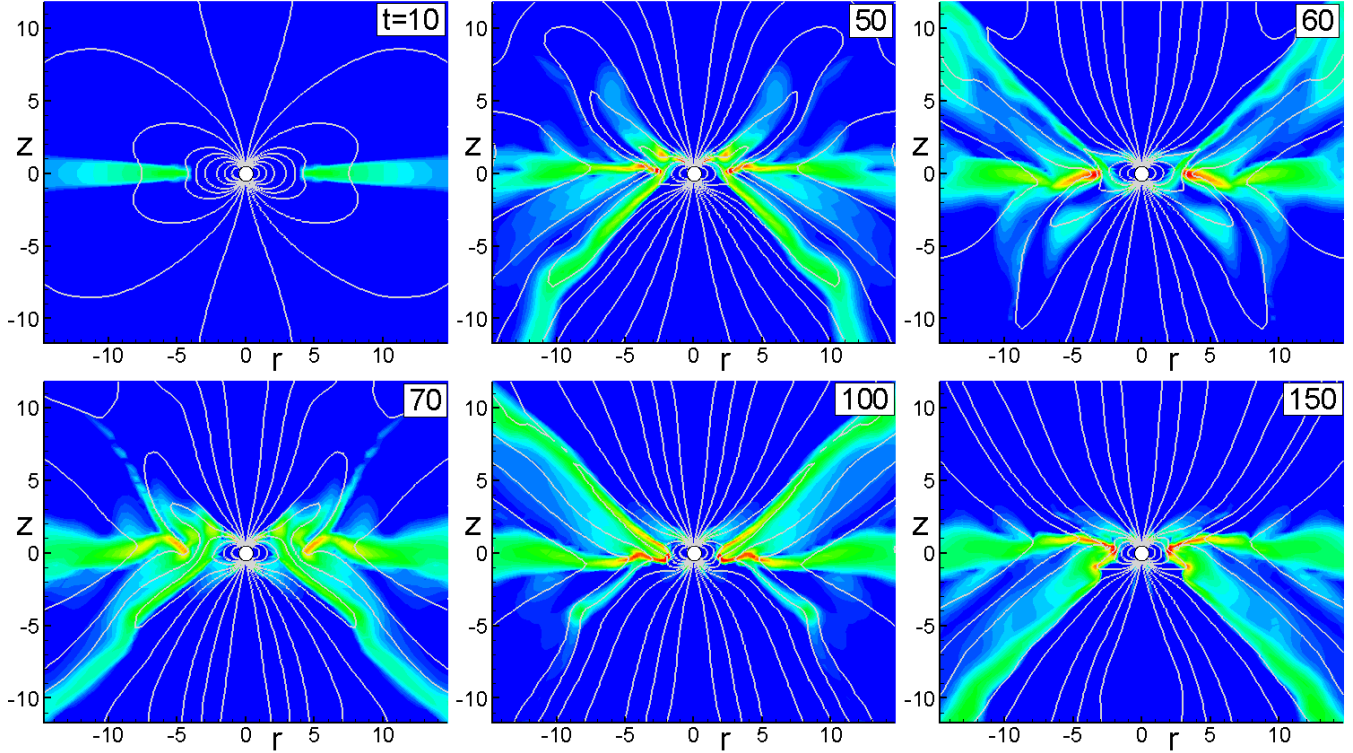


Figure 9. “Flip-flop” of outflows in case of a pure dipole field ($\tilde{\mu}_q = 0$, $\tilde{\mu}_d = 10$). Color background shows the matter flux distribution, and lines are the magnetic field lines.

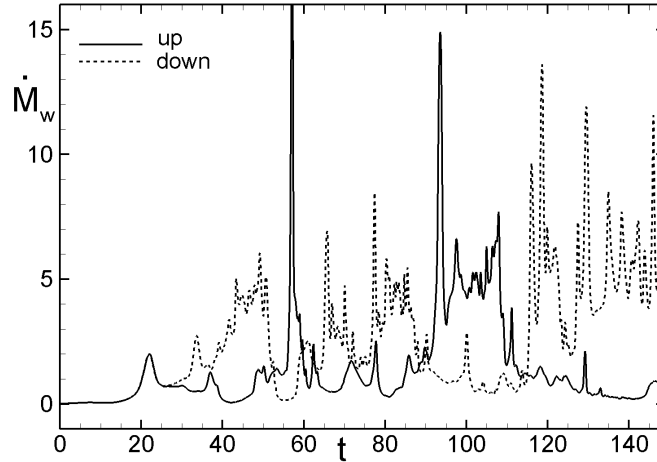


Figure 10. Matter fluxes calculated through the spherical radius $r = 10$ above the equatorial plane (solid lines) and below the equatorial plane (dashed lines) for the case of pure dipole field, $\tilde{\mu}_d = 10$ and $\tilde{\mu}_q = 0$.

and lower half-spaces. The star was assumed to be rapidly rotating with the magnetosphere in the propeller regime (U06). The ratio of the turbulent viscosity to the turbulent magnetic diffusivity in the disk was considered to be larger than unity so that the magnetic field threading the disk is advected inward (U06, R09). The main findings are the following:

1. For cases with both dipole and quadrupole components, a one-sided conical wind forms and persistently blows in one direction. The favored direction is that of larger magnitude intrinsic axial magnetic field. Much weaker outflows form on the opposite side of the disk.

2. For the case of a pure dipole field, the outflows are also one-sided, but the outflow direction alternates or “flip-flops” on a time-scale of about 30d for a T Tauri star. If the quadrupole component is small, $\tilde{\mu}_q = 1$, the behavior is similar to the case of $\tilde{\mu}_q = 0$.

3. For the case of a pure quadrupole field, symmetric outflows form. However, the presence of even very small dipole component leads to one-sided outflows.

Note, that outflows from a T Tauri star may change direction due to variations of the star’s magnetic field on a time-scale of months (Smirnov et al. 2004). If the complex field

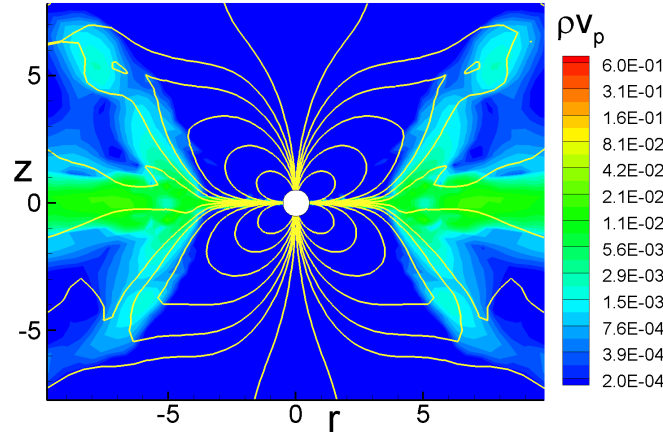


Figure 11. Matter flux-density for the case of a pure quadrupole field with $\bar{\mu}_q = 60$. The upward and downward outflows are approximately equal.

of a star is determined by dynamo processes inside the star, then one or another hemisphere may have the stronger axial magnetic field which determines the direction of the outflow.

An intrinsic asymmetry of the outflows or jets will give a net force on the protostar by analogy with the previously analyzed case of asymmetric jets from magnetized black-hole disks (Wang et al. 1992; Tsygan 2007; Kornreich & Lovelace 2008). If the outflow is one-sided for a long time T with asymptotic velocity V_j and mass flux \dot{M}_j , then the velocity imparted to the star is $\Delta v_* = \dot{M}_j V_j T / M_*$. For example, for a T Tauri star with $\dot{M}_j = 10^{-8} M_\odot \text{yr}^{-1}$, $V_j = 3 \times 10^7 \text{cm s}^{-1}$, $T = 10^5 \text{yr}$, and $M_* = M_\odot$, we find $\Delta v_* = 3 \times 10^4 \text{cm s}^{-1}$ which is probably undetectable. For the case of an almost pure dipole field the frequent “flip-flops” of the outflow direction will cause the star to random walk but the net displacement and velocity are very small.

In addition to the intrinsic stellar magnetic field considered here, the accretion disk can advect inward external (e.g., interstellar) magnetic flux because of the disk’s highly conducting (non-turbulent) surface layers (Bisnovaty-Kogan & Lovelace 2007; Rothstein & Lovelace 2008; Lovelace, Rothstein, & Bisnovaty-Kogan 2009). The combination of the advected field and the intrinsic field of the star can give rise to a complex field structure near the star’s magnetopause which produces asymmetric or one sided outflows. The field of the star may be dynamo generated with a complex time-dependent structure (e.g., von Rekowski & Brandenburg 2006). In the case of disk accretion to a black hole, a large-scale asymmetric magnetic field close to the black hole can arise from advection of external flux due to the conducting surface layers of the disk or it may arise from dynamo processes in the disk which generate both dipole and quadrupole field components (e.g., Pariev & Colgate 2007; Pariev, Colgate, & Finn 2007). Dynamo processes may also be important in the disks of accreting stars.

ACKNOWLEDGMENTS

We thank F. Bacciotti for a valuable discussion. This work was supported in part by NASA grants NNX08AH25G and NNX10AF63G and by NSF grant AST-0807129. MMR thanks

NASA for use of the NASA High Performance Computing Facilities. AVK and GVU were supported in part by grant RFBR 09-02-00502a, Program 4 of RAS.

REFERENCES

- Bacciotti, F., Eisloffel, J., & Ray, T.P. 1999, *A&A*, 350, 917
 Bisnovaty-Kogan, G.S., & Lovelace, R.V.E. 2007, *ApJ*, 667, L167
 Coffey, D., Bacciotti, F., Woitas, J., Ray, T.P., & Eisloffel, J. 2004, *ApJ*, 604, 758
 Donati J.-F., Jardine, M.M., Petit, P., Morin, J., Bouvier, J., Cameron, A.C., Delfosse, X., Dintrans, B., Dobler, W., Dougados, C., Ferreira, J., Forveille, T., Gregory, S.G., Harries, T., Hussain, G.A.J., Ménard, F., & Faletou, F. 2007a, in *ASP Conf. Ser., Proc. 14th Meeting on Cool Stars, Stellar Systems and the Sun. Astron. Soc. Pac. van Belle G., ed., (astro-ph/0702.0159)*
 Donati, J.-F., Jardine, M. M., Gregory, S. G., Petit, P., Bouvier, J., Dougados, C., Ménard, F., Cameron, A. C., Harries, T. J., Jeffers, S. V., Paletou, F. 2007b, *MNRAS*, 380, 1297
 Donati, J.-F., Jardine, M. M., Gregory, S. G., Petit, P., Paletou, F., Bouvier, J., Dougados, C., Ménard, F., Cameron, A. C., Harries, T. J., Hussain, G. A. J., Unruh, Y., Morin, J., Marsden, S. C., Manset, N., Aurière, M., Catala, C., Alecian, E. 2008, *MNRAS*, 386, 1234
 Goodson, A.P., & Winglee, R. M., 1999, *ApJ*, 524, 159
 Goodson, A.P., Winglee, R. M., & Böhm, K.-H. 1997, *ApJ*, 489, 199
 Goodson, A.P., Böhm, K.-H., Winglee, R. M. 1999, *ApJ*, 524, 142
 Jardine, M., Collier Cameron, A., & Donati, J.-F. 2002, *MNRAS*, 333, 339
 Kornreich, D.A., & Lovelace, R.V.E. 2008, *ApJ*, 681, 104
 Long, M., Romanova, M. M., & Lovelace, R. V. E. 2007, *MNRAS*, 374, 436
 ——— 2008, *MNRAS*, 386, 1274
 Long, M., Romanova, M.M., Lamb, F.K., 2009, *MNRAS*, arXiv:0911.5455
 Long, M., Romanova, M. M., Lamb, F., Kulkarni, A.K., & Donati, J.-F. 2010, *MNRAS*, in preparation

- Lovelace, R.V.E., Berk, H.L., & Contopoulos, J. 1991, *ApJ*, 379, 696
- Lovelace, R.V.E., Romanova, M.M., & Bisnovatyi-Kogan, G.S. 1999, *ApJ*, 514, 368
- Lovelace, R.V.E., Rothstein, D.M., & Bisnovatyi-Kogan, G.S. 2009, *ApJ*, 701, 885
- Pariiev, V.I., & Colgate, S.A. 2007, *ApJ*, 658, 129
- Pariiev, V.I., Colgate, S.A., & Finn, J.M. 2007, *ApJ*, 658, 129
- Romanova, M.M., Ustyugova, G.V., Koldoba, A.V., & Lovelace, R.V.E. 2005, *ApJ*, 635, 165L
- Romanova, M.M., Ustyugova, G.V., Koldoba, A.V., & Lovelace, R.V.E. 2009, *MNRAS*, 399, 1802 (R09)
- Rothstein, D.M., & Lovelace, R.V.E. 2008, *ApJ*, 677, 1221
- Shakura, N.I., & Sunyaev, R.A. 1973, *A&A*, 24, 337
- Shu, F., Najita, J., Ostriker, E., Wilkin, F., Ruden, S., Lizano, S. 1994, *ApJ*, 429, 781
- Smirnov, D. A., Lamzin, S. A., Fabrika, S. N., & Chuntunov, G. A., 2004, *Astron. Lett.*, 30, 456
- Tsygan, A.I. 2007, *Astron. Rep.*, 51, 97
- Ustyugova, G.V., Koldoba, A.V., Romanova, M.M., & Lovelace, R.V.E. 2006, *ApJ*, 646, 304 (U06)
- von Rekowski B., & Brandenburg A., 2006, *Astron. Nachr.*, 327, 53
- Wang, J.C.L., Sulkanen, M.E., & Lovelace, R.V.E. 1992, *ApJ*, 390, 46
- Woitak, J., Ray, T.P., Bacciotti, F., Davis, C.J., & Eislöffel, J. 2002, *ApJ*, 580, 336